Supporting Information for:

A new paradigm for battery structural design towards interface-free, all-in-one cell configuration

Weixing Xiong, Xueying Zheng, Yuchen Li, Zhang Cao, Jiayang Sun, Yan Wang, Linze Lv, Qunting Qu, Wei Luo and Honghe Zheng**

Experimental procedures

Material preparations: Boric acid (BA, Sinopharm Chemical Reagent Co., China) solution (2 wt%) is introduced into 20 g polyacrylic acid (PAA, 5 wt%, average MW=~3000 Da, Aladdin) solution at a molar fraction of 1:4 and the cross-linking between PAA chain *via* BA is induced at 80 °C condition. After thotoughly stirring for 16 hours, LiOH aqueous solution was introduced to adjust the pH value to 7.0 and the LiPAAOB solution is obtained. Then, 30 wt% polyethylene oxide (PEO, average MW=~7MDa, Aladdin) at a PEO/PAA ratio of 3:7 is incorporated into the LiPAAOB solution. After stirring for 2 hours, the LiPEAOB composite solution is obtained. Nano γ-Al_2O_3 (average diameter =~500 nm, Macklin Biochemical Co., China) was used as the inorganic filler, which was uniformly dispersed into the LiPEAOB composite solution. According to the amount of γ-Al_2O_3 used in the composite polymer (0%, 3%, 5%, 10% and 15%), the obtained samples are designated as LiPEAOB, LiPEAOB-Al3, LiPEAOB-Al5, LiPEAOB-Al10, and LiPEAOB-Al15, respectively. The LiPAAOB, LiPEAOB and LiPEAOB-Al10 films were prepared by casting each solution onto an 80*80 mm PTFE mold. The mold was then moved into a freezing drier at -50 ℃ for 24 hours. After proper rolling, the composite film of *ca.* 30 μm thickness was obtained.

Half-cell fabrications: The prepared LiPEAOB composite solution is adopted as the electrode binder for both $LiFePO_4$ (LFP) cathode and graphite anode. When used with the LFP cathode (C-coated, purchased by PylonTech. Co. Ltd), the slurry containing LFP, SP conductive carbon, and the LiPEAOB composite binder at a dry weight ratio

of 88:6:6 in water was homogenized under 10000 rpm for 30 min. Afterwards, the slurry was applied onto Al foil with doctor-blade coating. For comparison, the LFP cathode using the widely adopted PVDF binder in NMP is prepared according to the recipe of LFP:SP:PVDF=92:4:4. For the graphite anode, the electrode was prepared by casting the slurry consisting of an artificial graphite (BTR 918), LiPEAOB binder and SP at a dry weight ratio of 94:4:2 onto Cu foil. For comparison, the graphite anode using the widely adopted CMC/SBR binder is prepared according to the general recipe of graphite:SP:CMC:SBR=95:1.5:1.5:2. After oven drying, the obtained electrode laminate is rolled out and cut into discs of 13 mm diameter. The electrode discs were further dried under vacuum at 120 ^{o}C for 16 h and then transferred into an Argon-filled glove-box. The half cells (coin cell 2032) were assembled against Li foil with Celgard 2500 (PP) as the separator in 1_M $LiPF_6$ /EC: EMC: DMC (1:1:1) electrolyte.

All-in-one full cell fabrication: Firstly, the graphite slurry prepared with LiPEAOB binder was cast onto copper foil according to the above described recipes. Meanwhile, LFP slurry using the same LiPEAOB binder was casted onto Al foil. Before drying of the graphite anode and LFP cathode, the viscous LiPEAOB-Al10 solution is casted onto the graphite anode surface and the LFP cathode laminate is put onto the LiPEAOB-Al10 composite layer. To avoid the direct contact between the cathode and the anode, the obtained laminated structure was immediately moved into a freezing drier at -50 ^{o}C for 24 hours. Of course, the incorporated γ-Al_2O_3 also plays a role isolating the cathode with anode. After further drying under vacuum at 120 ^{o}C for 16

h, the all-in-one cell was assembled with 1 M $LiPF_6$ /EC: EMC: DMC (1:1:1) electrolyte, but without additional separator. The loading mass of LFP cathode is about 10mg/cm^2, and the N/P ratio is about 1.05.

Electrochemical tests: All the fabricated cells were formed and tested on a Neware CT-4008 cycler (Shenzhen, China). The voltage range for the graphite half-cell and the LFP half-cell was set at 0.005-1.5 V and 2.2-3.9 V, respectively. The voltage range of the full cells was set between 2.2 and 3.9 V. Rate capability was compared with the same charge/discharge rate ranging from 0.2 to 10 C, respectively. Cycling performance of the cells was evaluated at different charge and discharge rates. Cyclic voltammetry (CV) test of the cells was carried out on an Autolab potentiostat (Autolab Instruments, Switzerland) between 2.2 and 3.9 V at scan rates from 0.05 mV/s to 0.5 mV/s. Electrochemical impedance spectroscopy was collected on Zahner-Elektrik IM6 electrochemical workstation over the frequency range of 0.01 Hz to 100 kHz with an alternating voltage of 5 mV.

Material characterizations: Scanning electron microscopy (SEM) images of the samples were observed on Hitachi SU-8010 operated at 10 kV accelerating voltage. The chemical composition of the LiPAAOB, LiPEAOB and LiPEAOB-Al composite was identified using X-ray photoelectron spectroscopy (XPS) (Thermo Fisher, USA). The harvested samples were thoroughly dried under room temperature in vacuum before SEM and XPS measurements. Fourier transform infrared spectroscopy (FTIR) (TENSOR 27, BRUKER OPTICS, Germany) was conducted to investigate the functional groups of the LiPEAOB-Al composite. A thermal gravimetric analyzer

(DTA7300, SII Nanotechnology) was used to characterize the thermal stability of the obtained LiPEAOB-Al composite films. The desorption cumulative pore volume was measured by nitrogen adsorption/desorption isotherms using an automatic adsorption system (BET, ASAP2460, Norcross, GA, USA).

Figure S1 is the FTIR spectra of the BA, LiOH, PAA and the LiPAAOB composite polymer. A new peak at 1060 cm^{-1} corresponding to the -B-O-C vibration was seen after the addition of BA. It reveals that BA sets bridges between PAA chains. Meanwhile, an increase of the typical peak at 1570 cm^{-1} relating to the enhanced stretching vibration of the -COO group, indicating that similar to the lithium conduction mechanism of LiBOB, B-O bond can serve as a transport site for lithium ions along with the vibration of $–COO^-$ group.

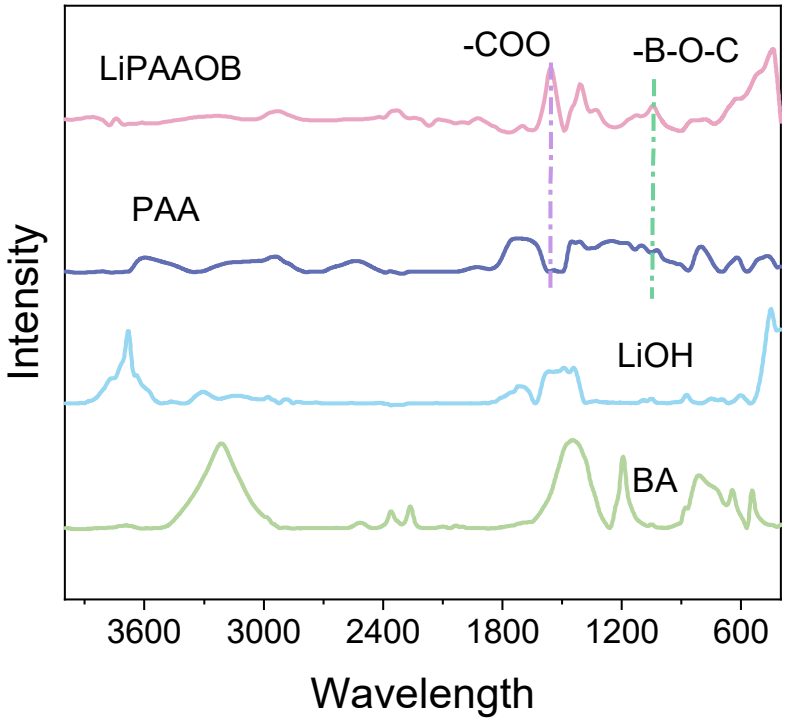

Figure S1. FTIR spectra of adopted BA, LiOH, PAA and the prepared LiPAAOB composite, respectively.

Figure S2 is the Nyquist plot for the Celgard 2500, LiPAAOB and LiPEAOB-Al films containing different amounts of nano γ-Al_2O_3 filler at 25 °C condition. The tests were done by EIS measurement sandwiched between two stainless steel sheets and sucked with 1M $LiPF_6$ in EC: EMC: DMC (1:1:1) electrolyte. Lithium-ion conductivity σ is calculated according to the equation σ=L/RS, where S is the area of the stainless steel, L is the thickness of electrolytes, and R is the intersection point of the diagonal line on the x-axis.

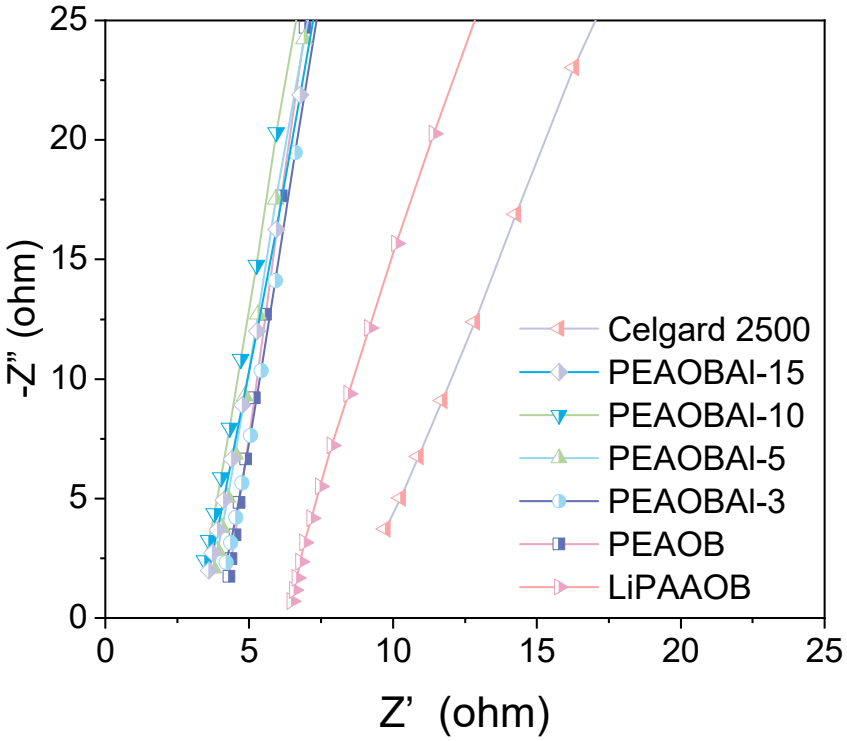

Figure S2. The impedance spectra collected from the Celgard 2500, LiPAAOB and the LiPEAOB-Al films containing different amounts of nano γ-Al_2O_3 filler at 25 °C.

Figure S3 shows the Li^+ transport mechanisms of the LiPAAOB, LiPEAOB and LiPEAOB-Al films. For LiPAAOB, boron serves as a transport site for lithium ions along with the vibration of $–COO^-$ group. For LiPEAOB, the enhanced vibration between boron ion and carbon-oxygen double bonds and multiplied ionic bonding between Li^+ and B-O brings fast lithium migration and sufficient Li transport sites. For LiPEAOB-Al film, nano-Al_2O_3 acts as reaction sites accelerate Li migration.

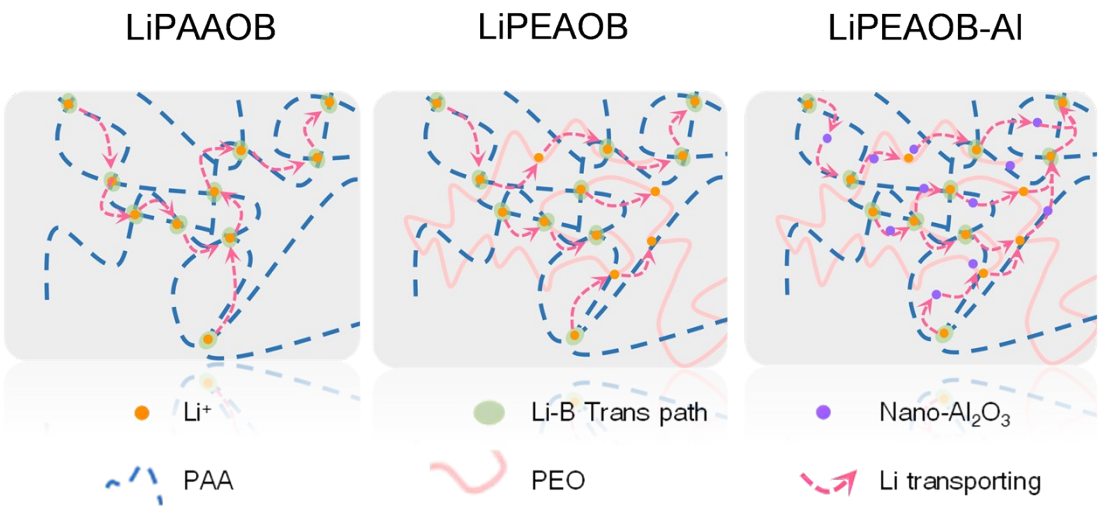

Figure S3. The diagrams for Li^+ transport mechanisms for the LiPAAOB, LiPEAOB and LiPEAOB-Al composite films.

Figure S4 compares the tensile strength of Celgard 2500, LiPAAOB and several kinds of LiPEAOB-Al films containing different amounts of nano γ-Al_2O_3 filler. The samples were cut into rectangular shape with a size of 3 × 6 cm^2. From this figure, the tensile strength of the LiPEAOBAl-10 film (19.4 MPa) is almost equivalent to that of the Celgard 2500 (PP) separator (around 27.9 MPa), showing satisfactory mechanical strength of the prepared LiPEAOB-Al10 film.

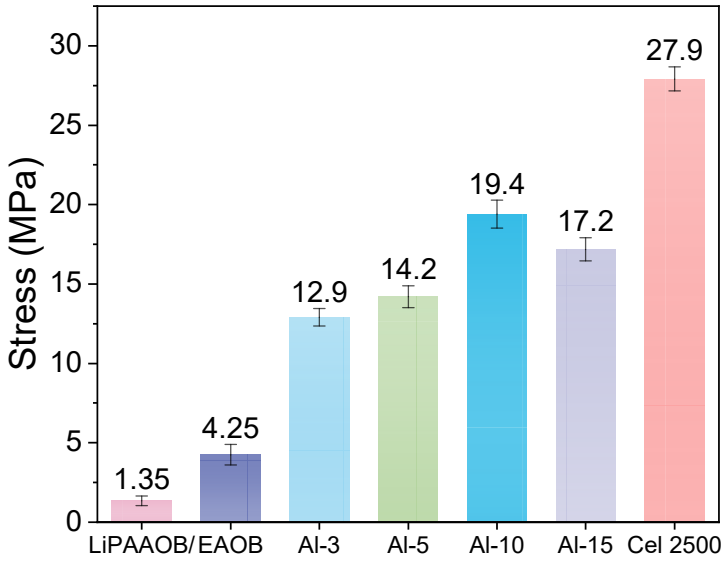

Figure S4. Comparison of the tensile strength between the Celgard 2500, LiPAAOB and LiPEAOB-Al films containing different amounts of nano γ-Al_2O_3.

Figure S5 displays the SEM image and the pore distribution of the prepared LiPEAOB-Al10 film. Different with the porous celgard 2500 film which containing *ca.*50% porosity, the porosity of the LiPEAOB-Al10 membrane is extremely low. On the one hand, the nonporous property makes it less demand for organic electrolyte, contributing to the battery safety. On the other hand, the nonporous film plays a role in reducing the cathode-anode cross-talk by blocking the passway between the cathode and the anode.

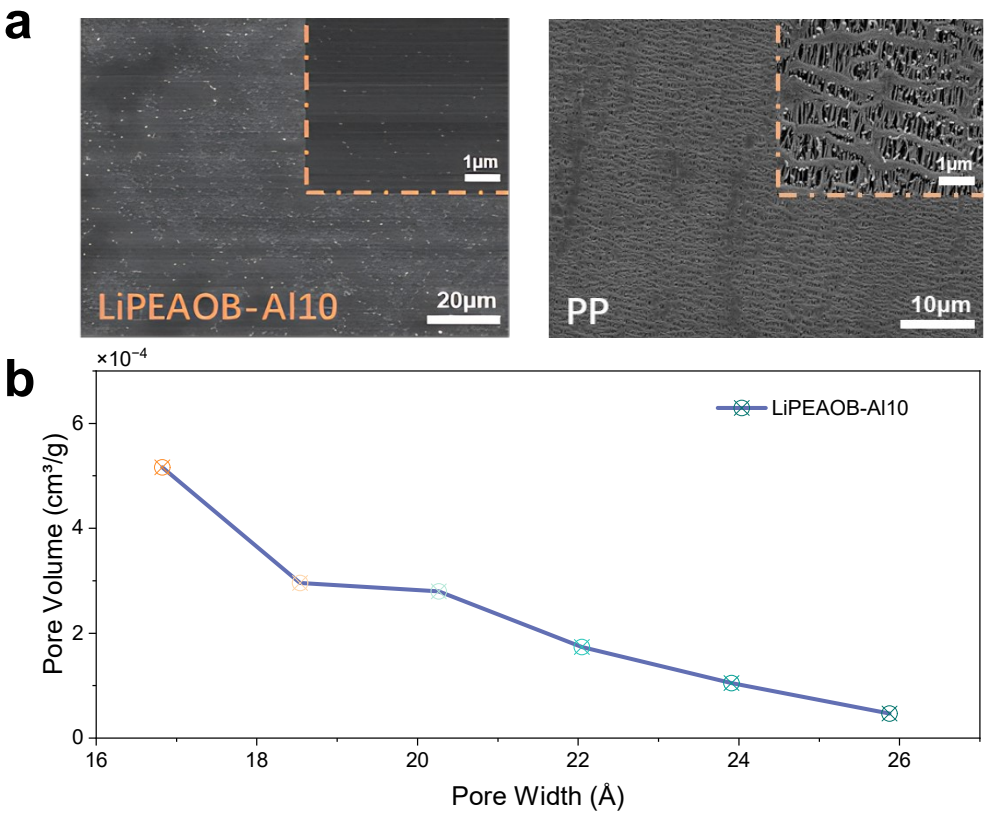

Figure S5. (a) SEM images of the prepared LiPEAOB-Al10 composite film and PP film with different resolutions. (b) The BJH desorption cumulative pore volume of LiPEAOB-Al10.

Figure S6 is the Nyquist plots of LFP electrode with PVDF and LiPEAOB binder after cell formation and after rate test, respectively. Obviously, the LFP cathode prepared with the LiPEAOB binder exhibits low impedance, especially after rate test. The fast kinetics explains the high rate capability of the LFP cathode using the functional LiPEAOB binder.

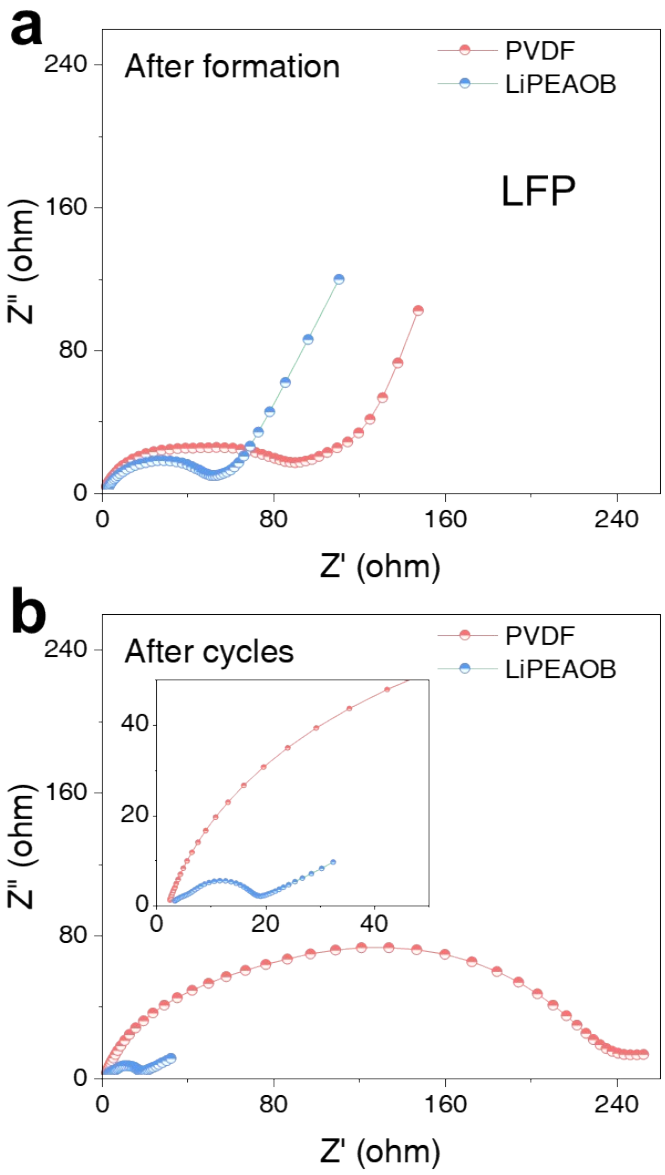

Figure S6. a-b, EIS profiles of the LFP electrode using traditional PVDF binder and the LiPEAOB binder after the cell formation (a) and after rate test (b).

Figure S7 is the Nyquist plots of the graphite anode using traditional CMC/SBR binder and the LiPEAOB binder after the cell formation and after rate test, respectively. It can be seen the graphite anode using the LiPEAOB binder shows low impedance compared to that using the traditional CMC/SBR binder.

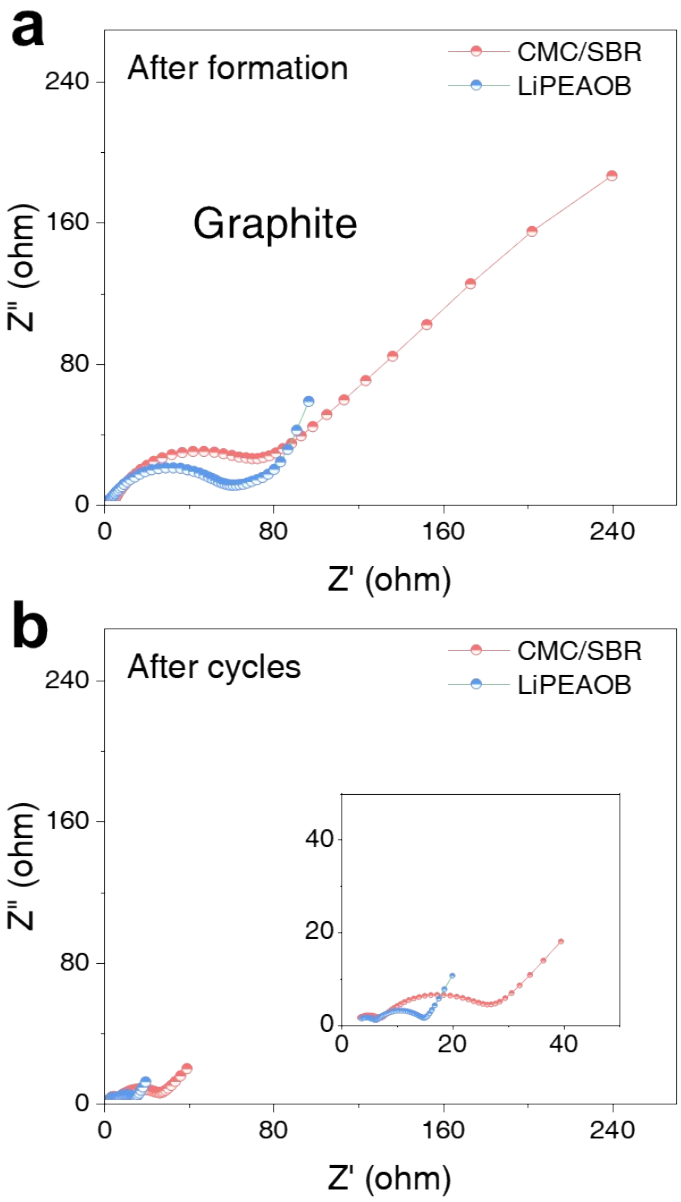

Figure S7. Nyquist plots of the graphite anode using traditional CMC/SBR binder and the composite LiPEAOB binder after cell formation (a) and after rate test (b).

Figure S8 compares the charge and discharge profiles of the laminated LBL cell and the integrated ALIB cell at different discharge rates. For the LBL cell, the lowering of the discharge curve at high rate is attributed to the high polarization induced by the high internal resistance of the cell. In contrast, with increasing discharge rate, the lowering of the discharge platform is not obvious for the interface-free ALIB cell, indicating an improved Li^+ migration within the cell.

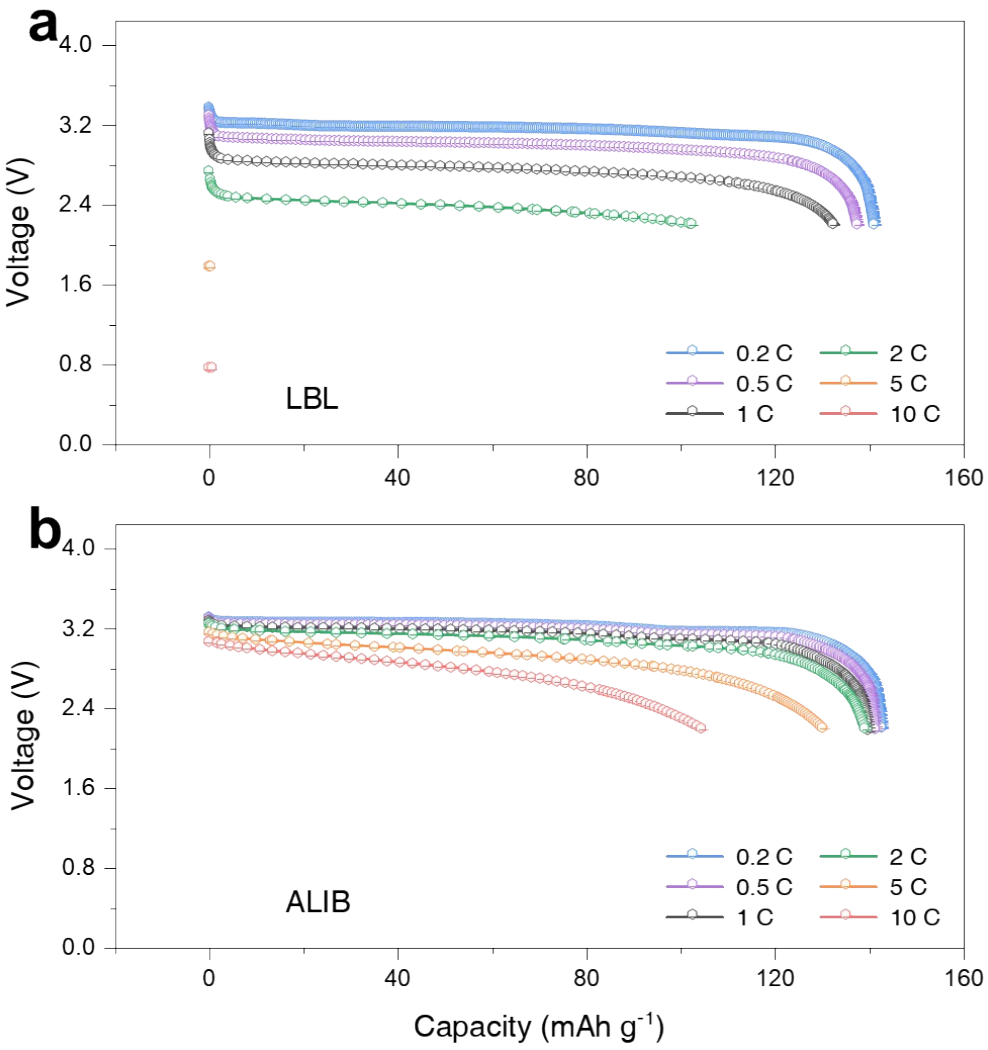

Figure S8. a-b, The discharge profiles for the laminated LBL cell (a) and the integrated ALIB cell (b) at different rates.

Figure S9 a, b display the Nyquist plots for the laminated LBL cell and the integrated ALIB cell after the cell formation and after 100 electrochemical cycles, respectively. Figure S9c shows the equivalent circuit for the Nyquist plots. The fitting results of R_{SEI} and Rct are compared in Figure S9d. Here it is seen that the R_{SEI} and R_{ct} of the integrated ALIB cell is significantly lower than those of the laminated LBL counterpart at different electrochemical cycles.

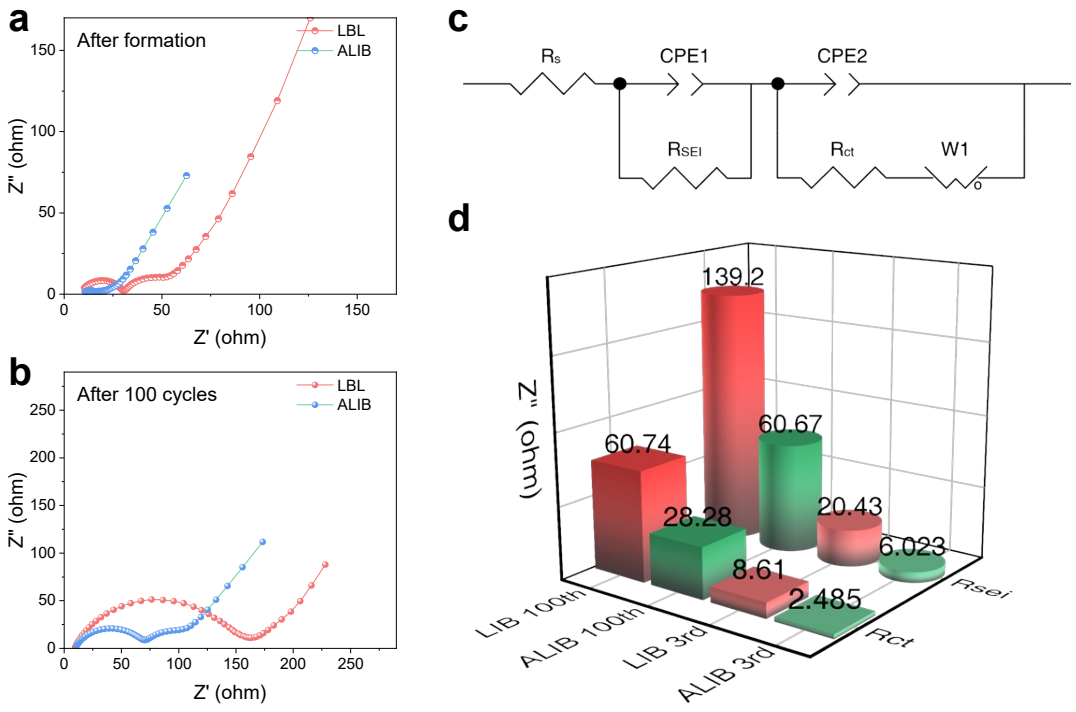

Figure S9. a-b, Nyquist plots of the laminated LBL cell and the integrated ALIB cell after the formation cycle (a) and after 100 cycles (b). c, The equivalent circuit for the Nyquist plots for fitting. d, R_{SEI} and Rct of the LBL cell and the ALIB cell after the cell formation and after 100 cycles.

Figure S10 presents the CV curves at various scan rates and the linear fitting between log(i) and log(v) for the laminated LBL cell and the integrated ALIB cell, respectively. With increasing scan rate from 0.05 to 0.5 mV/s, the shift of the peak position for the LBL cell toward high voltage is significantly higher than that of the ALIB cell. Correspondingly, a high b-value is obtained from the ALIB cell, indicating that the integrated ALIB cell has faster electrochemical kinetics.

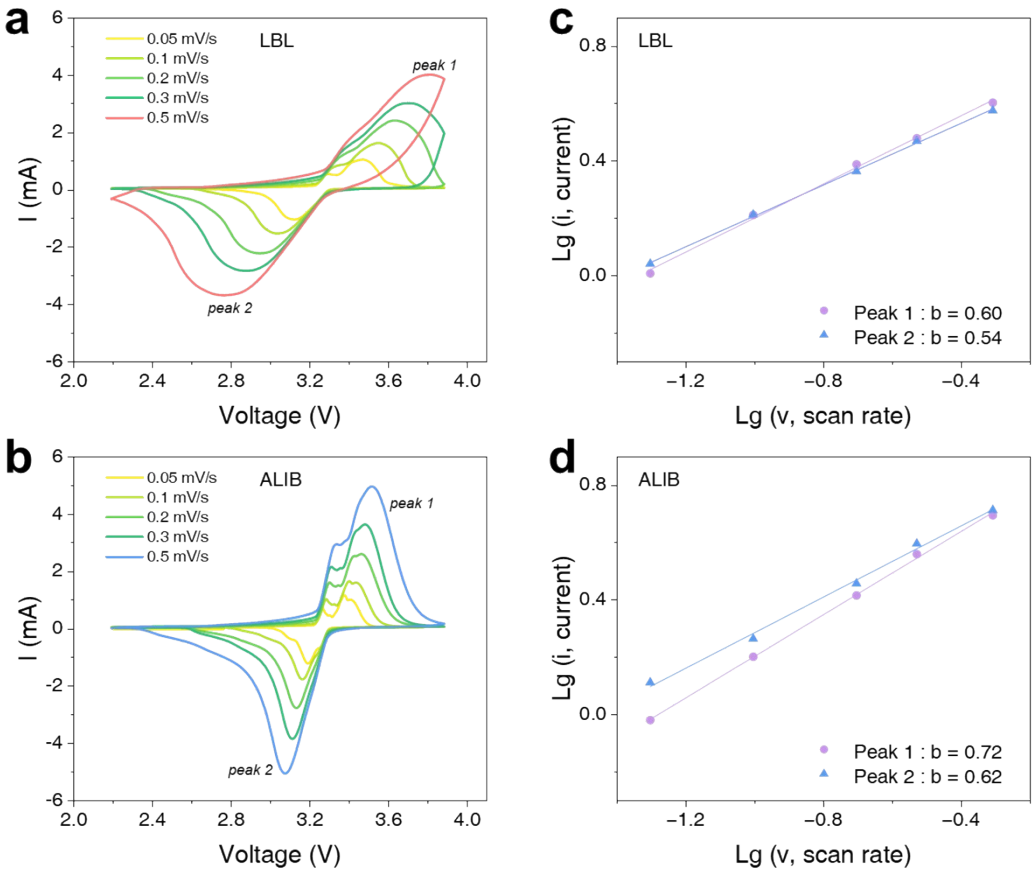

Figure S10. a-b, CV curves at various scan rates for the laminated LBL cell (a) and the integrated ALIB cell (b). c-d, The log-log plots between the peak current and the scan rate for the LBL cell (c) and the ALIB cell (d).

Figure S11 compares the 2 C charge and discharge profiles for the laminated LBL cell and the integrated ALIB cell at different electrochemical cycles. It is observed that, with increasing cycles, the gap between the charge and discharge platform for the LBL cell increases, meaning a continuous rise of the cell polarization. By contrast, the charge and discharge platforms for the ALIB cell are very stable, showing a stable internal structure of it.

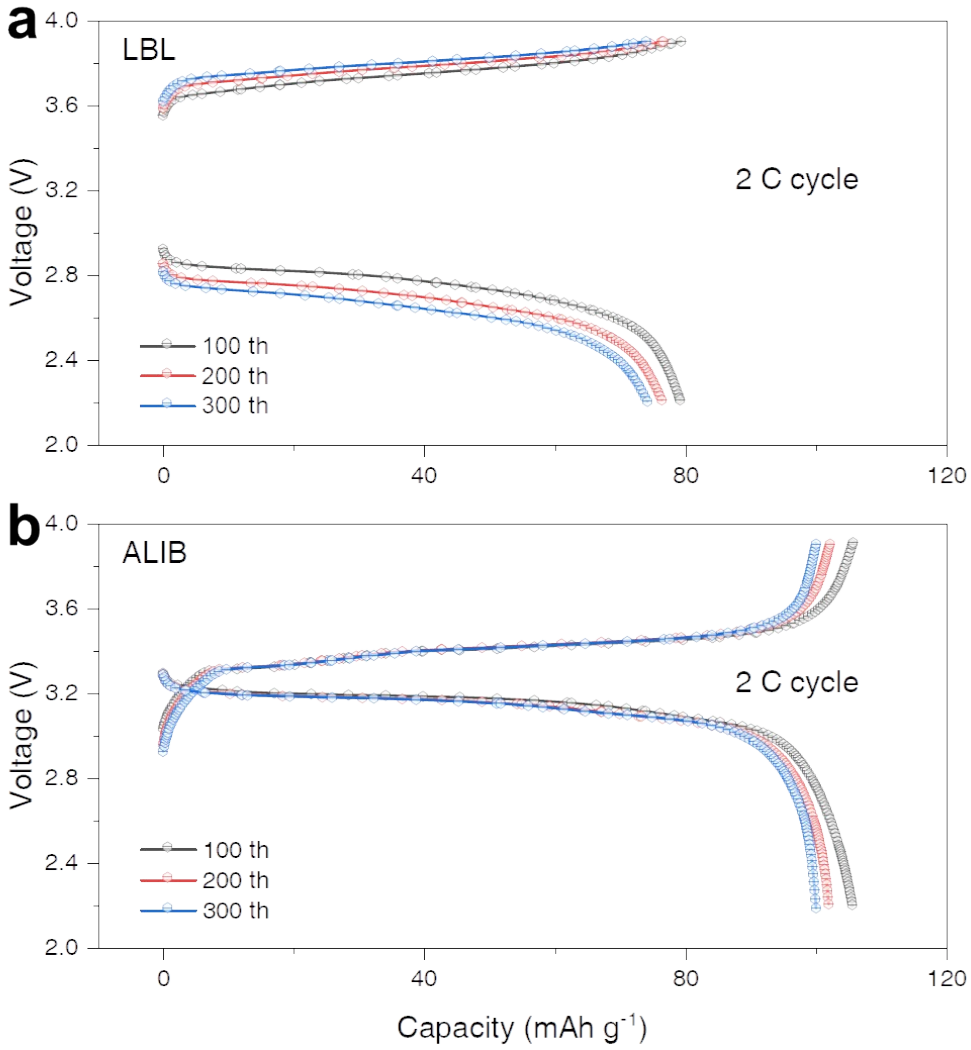

Figure S11. The 2 C charge and discharge profiles for the laminated LBL cell (a) and the integrated ALIB cell (b) at different electrochemical cycles.

Figure S12 is the cross-section SEM image of ALIB cell after 200 electrochemical cycles. After many electrochemical cycles, the continuous and seamless contact between the cathode, separator and the anode are well maintained. No misalignment between adjacent layers is detected and the nonporous LiPEAOB-Al10 separator turns to be more uniform and consistent. The very stable internal structure explains the long durability of the integrated ALIB cell.

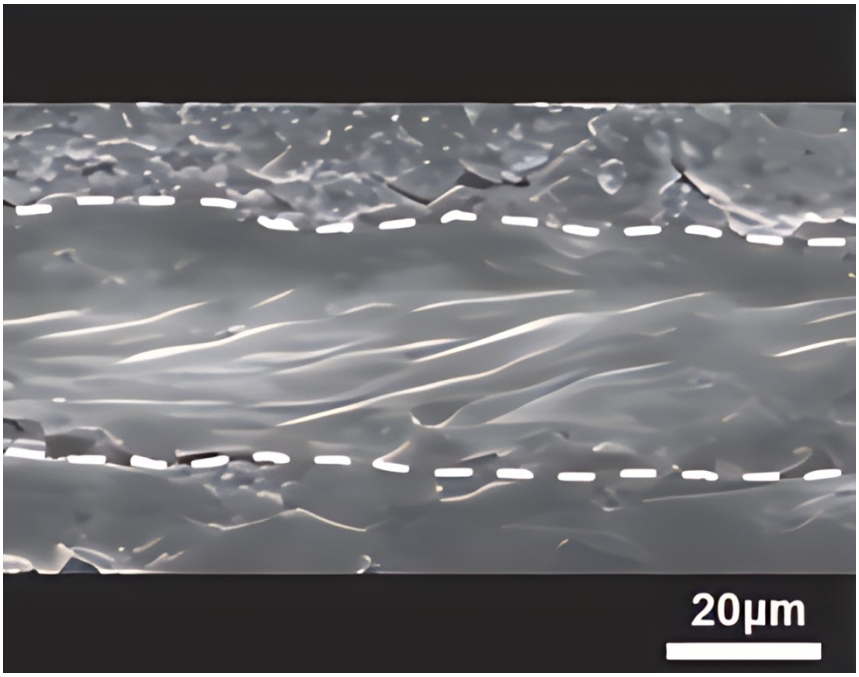

Figure S12. The cross-sectional SEM image of the interface-free ALIB cell after 200 cycles.

Figure S13 shows the SEM image and EDS mapping of the graphite electrodes harvested from the laminated LBL and the integrated ALIB cell after 200 electrochemical cycles. It is seen that there is much more Fe element on the graphite anode harvested from the LBL cell. The content of Fe element is calculated to be 2.47%, significantly high than that of 0.2% on the graphite anode collected from the integrated ALIB cell. This is a direct evidence for the reduced cathode-anode cross-talk by adopting the nonporous LiPEAOB-Al10 separator in the ALIB cell.

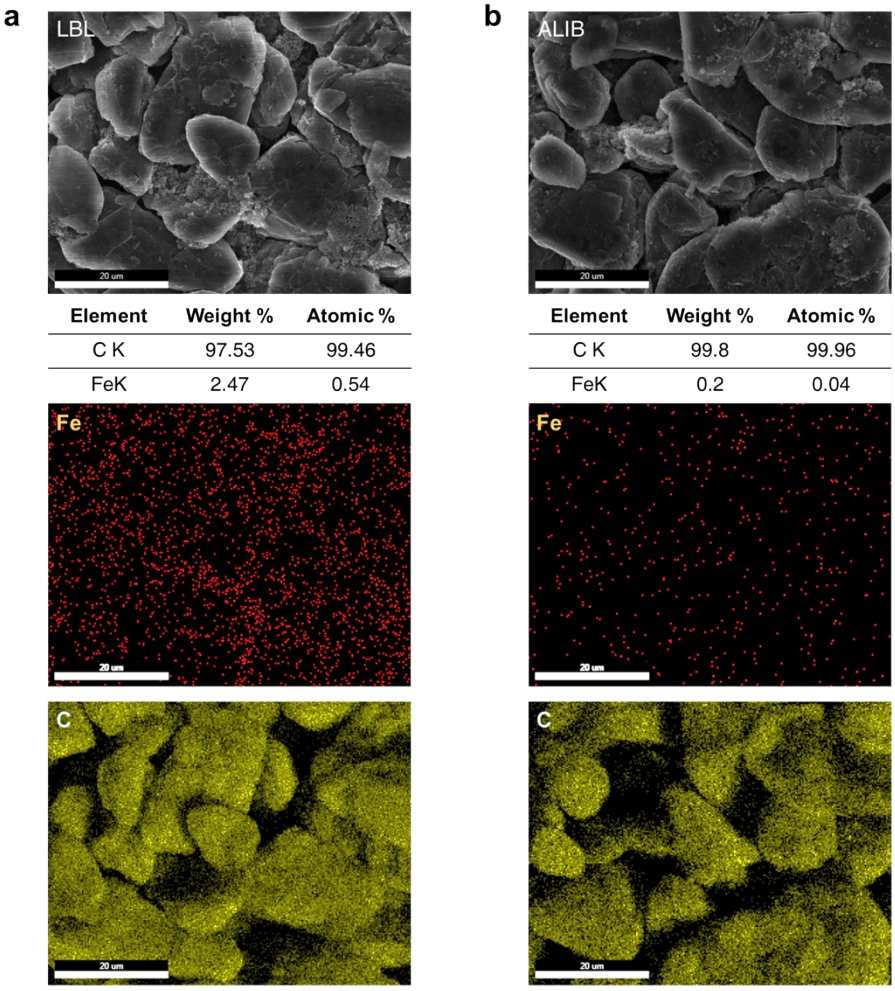

Figure S13. The SEM image and EDS mapping of graphite electrodes in the laminated LBL and the integrated ALIB cell after 200 electrochemical cycles.

Table S1: the ICP results of the Fe element on the post-cycled electrodes.

Sample	Element	Mean
LBL	Fe 238.204	0.276 mg/L
ALIB	Fe 238.204	0.043 mg/L